Improvement of the LLS and MAP deconvolution algorithms by automatic determination of optimal regularization parameters and pre-filtering of original data

Bruno Colicchio, Olivier Haeberlé, C. Xu, Alain Dieterlen, Georges Jung

Improvement of the LLS and MAP deconvolution algorithms by automatic determination of optimal regularization parameters and pre-filtering of original data

B. Colicchio, O. Haeberlé, C. Xu, A. Dieterlen

Groupe LabEl – Laboratoire MIPS, Université de Haute-Alsace

IUT Mulhouse, 61 rue A. Camus F-68093 Mulhouse Cedex France

G. Jung

Laboratoire d'Hématologie

Centre Hospitalier Emile Muller F-68093 Mulhouse Cedex France

Abstract:

We show that automatic determination of regularization threshold and pre-filtering of 3-D fluorescence microscopic images improves the stability of deconvolution results when using the Linear Least squares Solution or the Maximum a Posteriori method. Doing so, the choice of the regularization parameter much less depends on a priori knowledge of the specimen or skills of the operator. This increases the reliability and repeatability of quantitative measurements on deconvolved images.

Keywords: deconvolution, pre-filtering, 3-D microscopy

PACS numbers: 07.05.Pj; 42.30.Va; 07.60.P

1. INTRODUCTION

Fluorescence microscopy has proven to be an invaluable tool to study structures of living cells and tissues [1-3]. Recent developments in instrumentation [4-7] have permitted to beat the conventional Abbe limit, but for any acquisition instrument, each recorded image g(X) can be described by the following convolution equation:

$$g(X) = \int_{-\infty}^{+\infty} h(X - X_1) f(X_1) dX_1 \oplus b(X) \qquad (1)$$

where X and X_1 are 3-D coordinates, h(X) is the Point Spread Function (PSF) of the acquisition system and f(X) is the original object. The term b(X) represents a random process. It is a combination of noise sources due to the fluorescence process and the acquisition electronics. This equation expresses the fact that the original object is recorded with distorsions and blurring due to the finite resolution of the instrument, plus a contamination by noise. As a result, the acquired image is only an estimation of the original object, and may not be of high quality enough for post-acquisition analysis.

When the ultimate resolution is obtained from the instrument, it is still possible to sharpen the images by deconvolution of the data using the instrument point spread function. Deconvolution consists in inverting Eq. (1) in order to find a better estimate of the actual object f(X), knowing the image g(X) and the point spread function h(X). Deconvolution is known to be an ill-posed problem, the process being sensitive to initial conditions and noise. Furthermore, it can be very time consuming, especially for 3-D data sets and for iterative algorithms. A large amount of effort has been devoted to find new or improve existing deconvolution algorithms (Refs. [8-15] and references therein).

Deconvolutions techniques use a model of degradation induced by the imaging system. This model can be formulated by a linear convolution as in Eq. (1), or can be Bayesian, considering the image in a probabilistic way [16]. Many techniques have been investigated to achieve the restoration in spite of the ill-posed nature of the problem [17]. In the linear formalism, minimum mean-squares error restoration and least-squares filters methods model the image formation by a translation-invariant blurring contaminated with additive Gaussian noise. These methods can be computed in a direct form by the mean of Fast

Fourier Tansforms (FFT) computations. A classical implementation of these techniques is provided by the widely applied Wiener filter [18]. Another example is the Tikhonov-Miller algorithm, which uses a linear restoration filter, found minimizing the Tikhonov functional [19]. Verveer and Jovin [20] proposed an iterative constrained form of the Tikhonov-Miller algorithm, by implementing a non-negativity condition. Carrington also used the Tikhonov functional, but incorporated another non-negativity constraint for which he proved the unicity of the solution [13]. In the Bayesian formalism, a fluorescent object can be modeled as a spatially inhomogeneous Poisson process. The Richardson-Lucy algorithm [21] computes the maximum likelihood of this process. This method is closely related to the Expectation-Maximization algorithm and the Maximum Likelihood, Expectation Maximisation (ML-EM) method (see [11], [22,23] and references therein).

These methods are widely used by microscopists, as they are now available in commercial deconvolution packages, as well as some freely available softwares [24,25]. However, when large amounts of 3-D images are collected, the post processing of these data may constitute a bottleneck for the biologists if the computing time is too large. Unfortunately, the best deconvolution results are often obtained with time-consuming iterative algorithms like for example ML-EM and furthermore, not all deconvolved images appear to be of interest. A possible approach to this problem may be to implement a less accurate but rapid deconvolution method used to select the most interesting original images, which are then deconvolved with the better algorithms. This would limit the needed computation time.

In this view, we propose two improvements to the Linear Least squares Solution and the Maximum a Posteriori algorithms, which are based on direct matrix inversions, and therefore are fast, but sometimes instable. As a consequence, a regularization of the system to be inverted is mandatory for these two methods. We have implemented an automatic determination of the optimal regularization parameters, combined with a pre-filtering of the original data. Doing so, deconvolution results would not rely on parameters manually introduced by the operator and should be much less sensitive to noise, therefore diminishing the sensibility to a priori knowledge of the specimen and improving post-deconvolution quantitative measurements.

2. DECONVOLUTION ALGORITHMS

A large number of deconvolution methods have been described in the literature [8-9]. In this paper, we focus our attention on methods which suppose the knowledge of the image formation process, namely the Point Spread Function and are supposed to be well adapted to fluorescence microscopy: the LLS ("Linear Least Square" as implemented by C. Preza [10]) and the Maximum a Posteriori methods, which are based on direct inversion algorithms, and are therefore rapid compared to iterative algorithms like the ML-EM method ("Maximum Likelihood-Expectation Maximization" from Holmes [11-12]) or the algorithm of W.A. Carrington [13].

2.1 LLS : Linear Least Square

This algorithm [10] implies linear systems and restores data, which are contaminated by additive white gaussian noise. The reader interested in the mathematical foundations as well as the numerical implementation of this method will find more informations in [10,14,15]. We recall here only the fundamental concepts relative to this method. Equation (1) can be rewritten in discrete form as:

$$G = [H]\,F + B \qquad (2)$$

where G is the recorded image, F is the object, B represents the noise and [H] is a Toeplitz matrix representing the PSF. The system being singular or quasi-singular, the inversion of such a matrix is an ill-posed problem. Therefore regularization is needed. With the LLS algorithm, the lowest eigenvalues are simply discarded, and the operator has to manually introduce the regularization threshold β. Then Eq. (2) can be rewritten as:

$$\hat{F} = \left[H'^{t}\, H'\right]^{-1} H'^{t}\, G \qquad (3)$$

in which H' is the regularized H matrix.

2.2 MAP : Maximum a Posteriori

The photon statistics as detected by a CCD camera or a photomultiplier obeys the Poisson statistics [16]. Statistical image formation models therefore consider that the image is a convolution of the object f(x) by the PSF h(x) of the imaging system, but is formed randomly and therefore an acquired image is only a sample of this process taken at a given time t. The Bayesien model is based on the conditional statistics. The problem consists in maximizing the Probability Density Function of the object f with the knowledge of the image g. Conchello [26,27] proposed the following solution:

$$\hat{f} = \Phi_{MAP} g = \frac{H^*}{|H|^2 + \nu\left(\omega_x^2 + \omega_y^2 + \omega_z^2\right)} g \qquad (4)$$

with $\hat{f}$ being the reconstructed estimate of the original object, g the acquired image, H the Optical Transfer Function (the Fourier transform of the PSF); ω_x, ω_y, ω_z represent spatial frequencies in the image and ν is a regularization parameter to be introduced by the operator. The main difference with the LLS algorithms is that the smallest eigenvalues, which are simply discarded in LLS, are modified with ν in the MAP algorithm.

3. AUTOMATIC DETERMINATION OF REGULARIZATION PARAMETERS

Both LLS and MAP algorithms require a manual intervention to give these algorithms their respective regularization parameter. As a consequence, the results may greatly vary with the type of image or the signal to noise ratio, and therefore good deconvolution results strongly depends on the knowledge of the operator, and the result is judged qualitatively only.

At the Hematology Laboratory of Emile Muller Hospital (Mulhouse-France), a study of CD34+ cells from cord blood samples has been undertaken. Different populations appear during maturation of these cells and we would like to improve their classification method. This require the processing of relatively large populations (a few hundreds of cells) and therefore, use of fast deconvolution algorithms is mandatory. However, the quality of the image may vary, and automating the choice of the regularization parameter would greatly improve the quality and the reliability of the measurements, by discarding the necessity of a human intervention for choosing the “best” regularization parameters.

When optimizing deconvolution algorithms, one work first with synthetic image obtained by numerical convolution of a well-known reference object with a computed PSF. Then the result of the deconvolution may be compared with the original object.

When working on biological images, such a method cannot be used, as the original object is by definition what one would like to know. We have therefore introduced the following process, described by Figure 1. A known object **O** is numerically convolved with a PSF **H** to give an image **I**. This image is deconvolved with the regularized PSF **H'** to give an estimate of the object **O'**. Usually comparison of **O** and **O'** is used to perfect the choice of the regularization parameter. We propose to reconvolve **O'** with **H'** to give an estimate of the image **I'.** The original image **I** is compared with this simulated image. Doing so, we better mimic the real conditions of deconvolving an acquired image. Noise can also be added to test the robustness of the method.

Then, one varies the regularization parameter in order to obtain the best deconvolution results. We propose to use the Joyce and Root jauge [28,29] in order to get the best compromise (in the least square sense) between variance and bias. The variance and the bias error are linked to the eigenvalues, which are used for the inversion operation of the matrix system. When knowing the original object **O**, one minimizes the jauge:

$$F=\Sigma(O-O')^2 + \sigma^2\Sigma(1/\lambda_i) \qquad (5)$$

in which σ represents the power of the noise, which is usually estimated in a dark region of the original image, and the sum is computed with those eigenvalues, which have not been discarded (LLS) or modified (MAP). In practice, the original object is the unknown, and one starts with the deformed image of the object. Following Preza *et al.* [10], we use the same jauge but on the original image **I** and the estimated image **I'** in order to minimize:

$$F=\Sigma(I-I')^2 + \sigma^2\Sigma(1/\lambda_i) \qquad (6)$$

Alternatively, one can also use for F the quadratic error calculated between the original and restored object (when known), or between the original and the recomputed image (for biological images).

When working on noise-free synthetic images, we found these two criteria to work very well, giving very similar results than the conventional method using Eq. (5). However, the deconvolved image is very sensitive to noise, and applying this method on biological images often fails to give exploitable results. In order to use our automatic criterion on noisy images, we propose to use a pre-filtering of the original data.

4. PRE-FILTERING OF DATA

The original data as acquired on a microscope are always noisy. This noise is also responsible of instabilities in the inversion process. As a consequence, a trade-off between precision and stability has to be chosen. Pre-filtering the data permits to decouple the noise reduction process and the inversion process [30]. Pre-filtering increases the signal to noise ratio, and therefore simplifies the regularization process. One advantage of this approach is that one could consider an adaptative deconvolution scheme, in which the pre-filtering is adapted to the noise, and the inversion method is tuned with respect to the characteristics of the images and the type of measurements to be done, as some deconvolution algorithms give better results for shape reconstruction, and others for intensity measurements [31-33].

Using simulations we have first studied the influence of noise on the stability and precision of the solution, varying the level of noise to mimic typical images acquired on our fluorescence microscope.

We have built a synthetic object with 9 solid beads of same diameter but with different intensities (disposed in a cubic centered configuration). This object is convolved with a computed microscope PSF. We used the scalar Gibson and Lanni model of image formation [34], with parameters adapted to our microscope objective (see Annex 1, which details the parameters used in the Gibson and Lanni model as implemented in the XCOSM package for details [24]). More accurate vectorial models do exist [35,36], but this model has the advantage of clearly separating the various parameters characterizing the acquisition system: index of refraction of the immersion medium, coverslip index and thickness etc… For a more realistic simulation Gaussian noise is added. It corresponds to electronic noise due to the acquisition process. The fluorescence emission mechanism also implies Poissonian noise [37], for which better suited algorithms than MAP or LLS have been developed, however, when the signal to noise ratio is not too bad, LLS and MAP have proven to give good results. The relatively high noise level of 40% has been chosen as to mimic the noise observed in some biological images we acquired, and for which the LLS and MAP give useless results, as they fail to reconstruct the original data because of the noise. For such images, ML-EM gives good results. Our idea is to prefilter these images so as to render them usable with LLS or MAP, as they are faster methods, to permit a rapid screening of all images in order to select only the most interesting ones, which will then be treated with the more precise, more time consuming algorithms.

Figure 2 shows that the quadratic error curve with LLS deconvolution is very strongly depending on the regularization parameter β (note that the y-axis is on log scale): a small variation on the regularization parameter, as it would be manually introduced by the operator, would induce a large variation in the final result. Furthermore, according to the quadratic error criteria, even the best regularization parameter $\beta=10^{-2.7}$ fails to give a satisfactory result, as shown on Figure 3. The information is smeared out in the entire deconvolved image (Figure 3(a)), and no gain is obtained by deconvolution, for example for segmenting the image. Figure 3(b) shows the profile of a bead as measured on the deconvolved image (solid line) and compared to the original profile (dashed line). The restored intensity profiles are very different from the original one. This unsatisfactory result is due to the level of noise present in the original image. We propose to adapt to our 3-D images the approach proposed by Sekko [30], consisting in pre-filtering the original data in order to improve the quality of the deconvolution results.

The original data are pre-filtered with the transfer function:

$$W = \frac{1}{1+\alpha\cdot\dfrac{P_n(u,v,w)}{P_s(u,v,w)}} \qquad (3)$$

with $P_s(u,v,w)$ being the power spectrum of the signal and $P_n(u,v,w)$ being the power spectrum of the noise. The parameter α gives the level of filtering: for α=0 no filter is applied, α=1 corresponds to Wiener filter. Large values of α filter the noise but also the original data, therefore leading to loss of information.

These filtered data are then deconvolved using the MAP or LLS method. We have compared the results of without- and with pre-filtering restorations. To estimate the quality of deconvolution we compute the difference in the least-squares sense between the final data and the original object, which in that case is known.

To study the benefit of pre-filtering, we vary both parameters α (pre-filtering) and β (regularization threshold) and plot the 2-D corresponding error surface. As can be seen on Figure 4, a valley of stability is observed for a pre-filtering value of $\alpha=10^{-0.4}$ when using the LLS algorithm. In this valley (indicated by the arrow), the restoration error is much less sensitive to the choice of the regularization parameter, which can now vary over several decades without large changes in the deconvolved data. This result confirms for 3-D data the work of Sekko on 2-D images [21]. The minimum is observed for this image near $\alpha=10^{-0.4}$ and $\beta=10^{-4.3}$ and the deconvolution result for these values is shown on Figure 5. A 45% segmentation level shows that volumic measurements are affected by an error of 23% and intensity measurements are affected by an error of 20% with respect to the original image, indicating a good restoration despite the noise level, contrary to deconvolution without pre-filtering, which gives meaningless results (289% error on volume and 93% on intensity measurements) as one could foresee from Figure 3. Similar results are obtained using the MAP algorithm.

The proposed pre-filtering method is a common one, and because pre-filtering mutes the high frequency unstable components, it is not very surprising that the regularization is more stable. This is however precisely the goal of our method, to be applied to biological images (see next section). In that case, a common underlying hypothesis for deconvolution is that the biological object does not present sharp transitions (because of the diffusion of the fluorophores in the specimen) and as a consequence, its image shall not contain high frequencies, except for those due to the noise, which we want to suppress.

One can observe on Fig. 5 that some reconstructed profiles for the flat spheres present some dips. This is easily explained by the regularization process, which mutes the high frequency unstable components, which are precisely those necessary to reconstruct a square profile.

In order to investigate the effect of our method on the spectrum of the images, we have also considered an object composed of 9 spheres of same intensity, but different diameters. Figure 6(a) shows (with perspective) the object under study, composed of the 9 spheres located in a centered cubic configuration. Figure 6(a') shows the spectrum of this object. Frequencies along the x- and z-axis are represented. The frequencies are displayed with a logarithmic scale, in order to enhance the lower, high-frequency components, following the equation: $S_{log}=\log_{10}(1+30*abs(S))$, where S (for spectrum) is the FFT of the object.

Same PSF and noise level as for Fig. 5 have then been used to mimic the acquisition process. Figure 6(b) shows the object, convolved with the PSF. Blurring and z-elongation are clearly visible. On Figure 6(b'), the effect of the missing cone is clearly visible, the frequencies along the z-axis being cut-off, and the spectrum exhibiting the classical butterfly shape for a conventional microscope [33]. Figure 6(c) and 6(c') are Figure 6(b) and 6(b') with the addition of noise, respectively. The effect of noise is to blur even more the image, which translates itself in the spectrum as a relative decrease of the higher components, namely a loss of contrast in the spectrum.

Figures 6(d) to 6(f) show the results of LLS, MAP and ML-EM deconvolutions, respectively, with Figures 6(d') to 6(f') displaying the associated spectrums. Because of the noise, regularization for LLS and MAP deconvolution must be kept at a high level by discarding or lowering the unstable, higher-frequencies starting at a relatively low frequency. As a consequence, the z-elongation is weakly corrected only. This is clearly visible on the associated spectrums, as those frequencies which are present, but attenuated, in Figure 6(b') are indeed partially restored, but the missing cone is still clearly visible. Deconvolution with ML-EM gives slightly better results, as can be seen on Figure 6(f), for which the z-elongation is better corrected. On Figure 6(f'), one can clearly see this effect, as the missing cone present in Figures 6(b')(c') is now partially filled.

Figures 6(g) to 6(i) display the results of LLS, MAP and ML-EM deconvolutions, respectively, but now including our pre-filtering, technique, with Figures 6(g') to 6(i') displaying the associated spectrums. Comparing Figures 6(g) to 6(i) with Figures 6(d) to 6(f) shows that for the three deconvolution methods considered in this paper, a noticeable gain in the deconvolution results quality is obtained.

First, the objects (the 9 solid spheres) are better separated from the fuzzy background due to the noise, thanks to the pre-filtering. This results in an easier segmentation of the deconvolved images.

Second, because much of the noise is suppressed, the deconvolution algorithms can now better restore the higher frequencies, which permits a better reconstruction of the shapes. For our automatized LLS and MAP programs, this results in the inversion processes now being able to take into account more higher frequencies, which without filtering would otherwise contribute to amplify the noise to a catastrophic level, rendering the deconvolution useless.

The better quality of the results is clearly visible on Figures 6(g') to 6(i'), which compared to Figures 6(d') to 6(f'), show an extended reconstructed spectrum, ML-EM with pre-filtering being able to almost fully reconstruct the original spectrum.

Table 1 shows some quantitative measurements done on the deconvolved images presented in Figure 6. The nine solid spheres are presented in increasing size order. We focused our attention onto the volume, total (integrated over volume) intensity and maximum intensity for each sphere. All images are segmented in the same way, by applying a 15% threshold level, relatively to the maximum intensity in the image. The first lines (entitled Original) give the reference data for each sphere, which are supposed to be recovered after deconvolution. We considered LLS, MAP and ML-EM deconvolution, without- and with pre-filtering (called LLS+, MAP+ and ML-EM+ in Table 1), respectively. All results for deconvolved images are presented as variations in percentage with respect to the original spheres.

First, one should note that for the two smallest spheres, no relevant measurements could be done after deconvolution. The reason is that these smaller spheres are not properly segmented and are considered as smeared-out in the background. Note that in this work, we focus our attention onto improving the quality of the quantitative measurements, and not onto getting the highest possible separation or identification of small sources (resolution).

For volume measurements, pre-filtering increases the final results quality for all the three considered methods. For example, volume measurements with LLS+ show a typical 40% improvement over LLS. LLS+ and MAP+ give similar results in terms of sites identification and volume measurements. The best results in term of volume measurements are obtained with ML-EM+ with pre-filtering. Particularly interesting is that with this method, contrary to LLS+ or MAP+, the error on the volume not only is the lowest, but also shows little variations from one bead to the next. This also shows that ML-EM+ properly reconstructs the shapes, a conclusion which is supported by the fact that the object reconstructed with ML-EM+ has the closest spectrum to the original object made out of the 9 spheres (see Figure 6(a') and Figure 6(i')).

Integrated intensity measurements show a similar improvement for LLS+, MAP+ and ML-EM+ as well. The best results for the integrated intensity of each sphere are obtained with LLS+ (neglecting the bead ∅2), then MAP+. ML-EM+ with pre-filtering gives in that case worst results than ML-EM alone. This may be explained by the fact that ML-EM+ the best reconstructs the spheres with a correct shape and (almost) flat profile, but with a lower intensity than in the original object, which naturally translates as a similar error on the integrated intensity. Note however that the *variations of the errors* on the integrated intensity and the maximum intensity are also the lowest for ML-EM+, showing that this methods gives results which quality is almost independent of the size of the object.

For our biological applications, we are interested in identifying fluorescent sites on cells, for which we want to measure the integrated intensity of each fluorescent site, and its shape. One peculiar point of interest is to identify whether several types (in term of size and intensity) of fluorescent sites do exist, which may indicate different cell population. Consequently, making errors on the absolute level of fluorescence is not the most problematic, while correctly measuring the size and *relative* intensity of the fluorescent sites *on the same cell* is important.

As a conclusion of these simulations, we can choose either LLS+ or MAP+ for a first, rapid evaluation of the results, and then use ML-EM+ for a more precise estimation of (even) the *absolute* sizes (as ML-EM+ the best reconstructs the volumes) and *relative* maximum or integrated intensity (as ML-EM+ exhibits the lowest variations for this measurements).

5. APPLICATION TO BIOLOGICAL IMAGES

We then applied our pre-filtering method to biological images of CD34+ blood cord cells acquired with our BX51 epifluorescence microscope (Olympus), equipped with a CellScan 3-D acquisition device.

Images are acquired using a 12 bit, TE-1317-K Princeton CCD camera. Pixel size is 6.8x6.8 μm^2. A 100x, oil immersion (n_{oil}=1.515), NA=1.4 objective has been used in conjunction with coverglasses of design parameters (n_{glass}=1.525, 170 μm thickness). The PSF has been measured using TetraSpeck fluorescent latex beads of 0.2 μm diameter (Molecular Probes) (See Ref. [38] for details of the PSF acquisition protocol). The biological work on this cell line is to study possible population differentiation during the cell maturation. For this, one needs to study both the global fluorescence of the cell (for which deconvolution may be superfluous, because a conventional microscope, as opposed to a confocal microscope, transmits all the fluorescence light emitted by the cell, even in a fuzzy image) as well as the repartition of this fluorescence along some specific cell sites (for which deconvolution is mandatory) [39].

Figure 7 shows the results when deconvolving the data with and without pre-filtering and varying the regularization parameter for MAP deconvolutions. Figure 7(a) shows the original image. The level of noise in this image is compatible with a deconvolution without pre-filtering (α=0), as shown by Figures 7(b) and 7(c). However, changing the regularization parameter from $\beta=10^{-4}$ to $\beta=10^{-7}$ greatly changes the final result. This means that quantitative measurements (size of fluorescent sites for example) may greatly vary depending on the operator skills in fixing the value of β, which is beștsuited for a given image. On the contrary, when using a Wiener pre-filtering with α=1 and changing the regularization parameter β in the same range, the result of the deconvolution is much more stable, as shown by Figures 7(c) and 7(d).

We tested our method on several images for which, without pre-filtering, deconvolution failed or gave very different results with respect to the regularization parameter β and found it very reliable: in each case, the result of the deconvolution with pre-filtering is very insensitive to a large variation of β. For biological samples, the level of noise is estimated from the data by analyzing a supposedly signal-free region of the image.

We therefore can say that using a Wiener pre-filtering improves the deconvolution process with LLS and MAP in two ways. First, images one otherwise cannot deconvolve with a satisfactory result may now be used for biological measurements. Secondly, by eliminating the manual adjustment of the regularization parameter by the operator, the reliability and repeatability of the quantitative measurements on the deconvolved image is greatly improved. We believe this is an important step for having deconvolution methods more widely adopted for routine use by non-specialists of image processing.

When it comes to speed, our pre-filtering method combined with automatic determination of the optimal parameters for LLS or MAP also presents some advantages. The ML-EM deconvolution algorithm always gives the best results for our simulated as well as real biological images. However this method being iterative, it is rather time consuming, especially for large images. This is not real problem when only few images are to be treated. For our study of CD34 cells maturation [39], and in order to obtain statistically significant results, we have to process a few hundredths raw 3-D images, out of them a few dozens being biologically relevant are selected. Processing all images with ML-EM would be unrealistic in that case, as processing is much more longer than the sample preparation and data acquisition. Our methods give slightly lower quality results, but are faster.

Typically, for our CD34 images correct deconvolution results are obtained with ML-EM after about 100 iterations, which take about 35 mn per image on a 700Mhz Pentium III computer with 768 Mbytes of RAM. Our method permits to preprocess one 3-D image within 4 mn with LLS after 35 iterations and 8 mn with MAP after 27 iterations, in order to find the optimal regularization thresholds. We therefore use our improved LLS or MAP algorithm for a first, rapid screening of the deconvolved data, which permits to eliminate most of the biologically irrelevant images. Only the best raw candidates are then, in a second step, deconvolved with ML-EM before the biological analysis. Doing so greatly speeds up and facilitates the analysis work for the biologists.

6. CONCLUSION AND PERSPECTIVES

We have extended the technique proposed by Sekko [30] to 3-D biological images. We have shown that using a Wiener filter to pre-filter fluorescence images from an optical microscope greatly enhances the quality of the deconvolution and the reliability and repeatability of quantitative measurements. The result is then much less dependent on the regularization parameter used in the LLS or MAP deconvolution methods. This should help the biologists to use deconvolution techniques for their work.

Our method applied to the LLS and MAP deconvolution techniques recalls the results obtained by Van Kempen *et al.* on the Richardson-Lucy algorithm [40].

The method we propose has been tested on images from a classical microscope, but should also help to process images from confocal or bi-photon microscopes. The Wiener filter, which has been used in this work, is best suited for additive Gaussian noise. However, fluorescence emission is known to be also affected by Poissonian noise, so other type of pre-filtering may be used.

Finally, we have shown that pre-filtering can also improve deconvolution of noisy data sets with other algorithms like Maximum Likelihood-Expectation Maximisation (ML-EM). The Projection onto Convex Sets (POCS) method could also take benefit of this technique.

ANNEX 1

List of the parameters used to compute the PSF of a classical (non-confocal) fluorescence microscope with the XCOSM package:

Nxy: 128	size of the image in x and y
deltaxy: 0.068	pixel size in image space in µm
Nz: 64	size of the image in z (optical axis)
deltaz: 0.068	pixel size in z in µm
mag: 100	lateral magnification
NA: 1.4	numerical aperture of the objective
workdist: 0.16	working distance of the objective in mm
lamda: 0.000530	fluorescence wavelength in mm
slipdesri: 1.525	coverslip design refractive index
slipactri: 1.525	coverslip actual refractive index
slipdesth: 0.170	coverslip design thickness in mm
slipactth: 0.170	coverslip actual thickness in mm
medesri: 1.515	immersion oil design refractive index
medactri: 1.515	immersion oil actual refractive index
specri: 1.33	specimen refractive index
specthick: 0.0	specimen depth in mm
desot: 160	design tube length in mm
actot: 160	actual tube length in mm

REFERENCES

[1] T. Wilson and C.J.R. Sheppard *"Theory and practice of Scanning Optical Microscopy"* Academic Press, London (1984)

[2] D.A. Agard, Y. Hiraoka, P. Shaw and J.W. Sedat in *"Methods in Cell Biology, Fluorescence Microscopy in Three-Dimensions Vol. 30"* p. 353, D.L. Taylor and Y. Wang eds., Academic, San Diego, Calif. (1989)

[3] S. Hell, E. Lehtonen and E.H.K. Stelzer, in *"New Dimensions of Visualization in Biomedical Microscopies",* p. 145, A. Kritte ed., Verlag Chemie, Weinheim, Germany (1992)

[4] D. Minsky, Scanning **10**, p. 128 (1988)

[5] W. Denk, J.H. Strickler and W.W. Webb, Science **248**, p. 73 (1990)

[6] S. Hell and E.H.K. Stelzer, Opt. Comm. **93**, p.277 (1992)

[7] T.A. Klar and S.W. Hell, Opt. Lett. **24**, p. 954 (1999)

[8] B.R. Hunt, Inter. J. of Mod. Phys. C **5**, p. 151 (1994)

[9] E.S. Meinel, J. Opt. Soc. Am. **3**, p. 787 (1986)

[10] C. Preza *et al.*, J. Opt. Soc. Am. A **9**, p. 219 (1992)

[11] T.J. Holmes, J. Opt. Soc. Am. A **5**, p. 666 (1988)

[12] T.J. Holmes, J. Opt. Soc. Am A **8**, p. 893 (1991)

[13] W.A. Carrington, proc. SPIE **1205**, p. 72 (1990)

[14] C. Preza, M.I. Miller and J.-A. Conchello, proc. SPIE **1905**, p. 129 (1993)

[15] J.G. M^{c}Nally *et al.*, J. Opt. Soc. Am. A **11**, p. 1056 (1994)

[16] J.W. Goodman, *Statistical Optics*, John Wiley & Sons, New-York (1985)

[17] B.R. Hunt, J. Mod. Phys. **5**, p. 151 (1994)

[18] N. Wiener, *Extrapolation, interpolation and smoothing of Stationary Time Series*, MIT Press, Cambridge (1943)

[19] A. N. Tikhonov and V. Y. Arsenin, *Solutions of Ill-Posed Problem,* Halsted Press, Washington (1977)

[20] P. J. Verveer and T. M. Jovin, J. Microsc., **188**, p. 191 (1997)

[21] W.H. Richardson, J. Opt. Soc. Am. **62**, p. 55 (1972)

[22] A.P. Dempster, N.M. Laird and D.B. Rubin, J. R. Statist. Soc. **B39**, p. 1 (1977)

[23] L.A Shepp and Y. Vardi, IEEE Trans. Med. Imaging **1**, p. 113(1982)

[24] XCOSM: http://www.essrl.wustl.edu/~preza/xcosm/

[25] ImageTrak:
http://www.ohri.ca/programs/neuroscience/White_Matter_Injury/stysWeb/stysImageTrak.htm

[26] J.A. Conchello, "Three-dimensional reconstruction of noisy images from partially confocal scanning microscope", Ph.D. dissertation (Dartmouth College, Hanover, N.H., 1990)

[27] J.A. Conchello and E.W. Hansen, App. Opt. **29**, p. 3795 (1990)

[28] L.S. Joyce and W.L. Root, J. Opt. Soc. Am. A. **1**, p.149 (1984)

[29] W.L. Root, J. Opt. Soc. Am. A. **4**, p.171 (1987)

[30] E. Sekko, G. Thomas and A. Bourkrouche, Signal Proc. **72**, p. 23 (1999)

[31] P.J. Verveer and T.M. Jovin, J. Opt. Soc. Am. A **14**, p. 1696 (1997)

[32] P.J. Verveer and T.M. Jovin, J. Opt. Soc. Am. A **15**, p. 1077 (1998)

[33] A. Chomik *et al.*, J. Opt. **28** p. 225 (1997)

[34] S.F. Gibson and F. Lanni, J. Opt. Soc. Am. A **8**, p. 1601 (1991)

[35] P. Török, P. Varga, Z. Laczik and G.R. Booker, J. Opt. Soc. Am. A **12**, p. 325 (1995)

[36] S. Hell, G. Reiner, C. Cremer and E.H.K. Stelzer, J. Microsc. **169**, p. 391 (1993)

[37] D. Axelrod, Biophys. J. **26**, p. 557 (1979)

[38] O. Haeberlé *et al.*, Opt. Comm. **196**, p. 109 (2001)

[39] G. Jung *et al.*, "Three-Dimensional CD34 Antigen Expression in Human Umbilical Cord Cells", 45th American Society of Hematology Annual Meeting, 6-9 December 2003, San Diego, California, Blood **100**, p. 833 (2003).

[40] G.M.P Van Kempen, L.J. Van Vliet, P.J. Verveer and H.T.M. Van Der Voort, J. Microsc. **185**, p. 354 (1996)

TABLE CAPTIONS

Table 1: Quantitative measurements relative to the results presented in Figure 6. The 9 objects of increasing size are segmented, and their volume, total (integrated) intensity and maximum intensity are measured after LLS, MAP and ML-EM deconvolution, without- and with pre-filtering, respectively. All results for deconvolved images are presented as variations in percentage with respect to the original objects.

		Bead ∅1 (0.068µm)	Bead ∅2 (0.136µm)	Bead ∅3 (0.204µm)	Bead ∅5 (0.340µm)	Bead ∅6 (0.408µm)	Bead ∅7 (0.476µm)	Bead ∅8 (0.544µm)	Bead ∅10 (0.680µm)	Bead ∅11 (0.748µm)
Original	Volume (voxels)	1	7	27	81	115	251	341	515	739
	Σ(I)	100	700	2700	8100	11500	25100	34100	51500	73900
	Max(I)	100	100	100	100	100	100	100	100	100
LLS	ΔVolume	x	x	266.7	232.0	226.0	157.0	157.7	162.3	133.8
	ΔΣ(I)	x	x	-21.4	2.7	7.6	3.0	3.9	8.5	7.0
	ΔMax(I)	x	x	-63.3	-39.4	-26.7	-1.6	7.6	-0.6	-3.3
MAP	ΔVolume	x	x	207.4	258.0	247.8	211.6	186.7	168.8	148.7
	ΔΣ(I)	x	x	-39.6	-6.1	-0.5	7.2	7.2	8.0	7.4
	ΔMax(I)	x	x	-72.4	-47.2	-36.6	-15.7	-6.1	-4.0	-1.4
MLEM	ΔVolume	x	x	x	0	69.6	96.0	88.9	84.9	87.7
	ΔΣ(I)	x	x	x	-74.0	-47.7	-26.6	-23.8	-19.6	-15.1
	ΔMax(I)	x	x	x	-56.7	-23.2	-7.4	8.4	9.5	18.9
LLS+	ΔVolume	x	171.4	174.1	155.6	131.3	107.6	103.8	87.0	79.7
	ΔΣ(I)	x	-49.9	-8.7	-1.9	-5.1	-0.4	-1.4	-0.9	-0.7
	ΔMax(I)	x	-73.7	-33.3	-3.4	-6.6	-6.5	-5.5	-2	1.6
MAP+	ΔVolume	x	x	174.1	155.6	153.9	117.1	121.1	106.0	96.5
	ΔΣ(I)	x	x	-31.3	-10.4	-9.7	-5.1	-3.0	-1.9	-1.1
	ΔMax(I)	x	x	-58.0	-19.8	14.3	-5.5	-3.2	-4.6	-2.7
MLEM+	ΔVolume	x	x	-7.4	-8.6	7.8	9.6	4.1	14.0	9.1
	ΔΣ(I)	x	x	-52.3	-39.8	-29.7	-23.6	-23.8	-18.4	-19.3
	ΔMax(I)	x	x	30.1	78.2	46.6	39.8	38.1	43.8	40.8

Table 1

FIGURE CAPTIONS

Fig. 1: Scheme of automatic determination of the regularization parameter of the LLS or MAP algorithms. The original image is compared with a simulated image, which is obtained by re-convolution of the deconvolution result by the regularized PSF. Minimizing a functional F permits to choose the optimum regularization parameter without a priori knowledge of the operator. The figure shows x-y (top) and x-z (bottom) cuts of the 3-D data sets.

Fig. 2: Quadratic error curve computed between the original test data set and the deconvolved data set as a function of the regularization parameter β for the LLS algorithm. The error varies very fast with β.

Fig. 3: Best deconvolution result for our test data set computed at the minimum of the error curve of Figure 2. (a) deconvolved image (x-y and x-z cuts): the information has been smeared out in the noise. (b)-(c) profile cuts in the deconvolved image (solid lines) compared to profiles in the original images (dashed lines).

Fig. 4: Quadratic error surface computed between the original test data set and the deconvolved data set as a function of the regularization parameter β and the Wiener pre-filtering parameter α. Note the deep valley close to $\alpha=10^{-0.4}$: for this pre-filtering value, the deconvolution result is much less sensitive to β.

Fig. 5: Best deconvolution result for our test data set computed at the minimum of the error surface of

Figure 3. (a) deconvolved image (x-y and x-z cuts). (b)-(c) profile cuts in the deconvolved image (solid lines) compared to profiles in the original images (dashed lines). The quality of the reconstruction is greatly improved by pre-filtering.

Fig. 6: Application of LLS, MAP and ML-EM to a simulated image of an object consisting of 9 solid spheres of same intensity and different diameters. (a) original object viewed in perpective. (a') spectrum of the original object along the x- and z-axis. (b) object convolved with the PSF computed using the parameter of Annex 1. (b') spectrum of image (b). (c) et (c') same as (b) and (b') after addition of noise. (d) and (d') deconvolution of (c) with LLS and its spectrum. (e) and (e') deconvolution of (c) with MAP and its spectrum. (f) and (f') deconvolution of (c) with ML-EM and its spectrum. (g) and (g') deconvolution of (c) with LLS with pre-filtering and its spectrum. (h) and (h') deconvolution of (c) with MAP with pre-filtering and its spectrum. (i) and (i') deconvolution of (c) with ML-EM with pre-filtering and its spectrum.

Fig. 7: Application to a typical 3-D biological image. (a) original data. (b) without pre-filtering MAP deconvolution with $\beta=10^{-4}$. (c) without pre-filtering MAP deconvolution with $\beta=10^{-7}$. (d) Wiener pre-filtering with $\alpha=1$ and MAP deconvolution with $\beta=10^{-4}$. (e) Wiener pre-filtering with $\alpha=1$ and MAP deconvolution with $\beta=10^{-7}$. Pre-filtering stabilizes the deconvolution process and measurements on Figure 6(d)-(e) are more reliable than measurements on Figure 6(b)-(c). The figures show x-y (top) and x-z (bottom) cuts of the 3-D data sets.

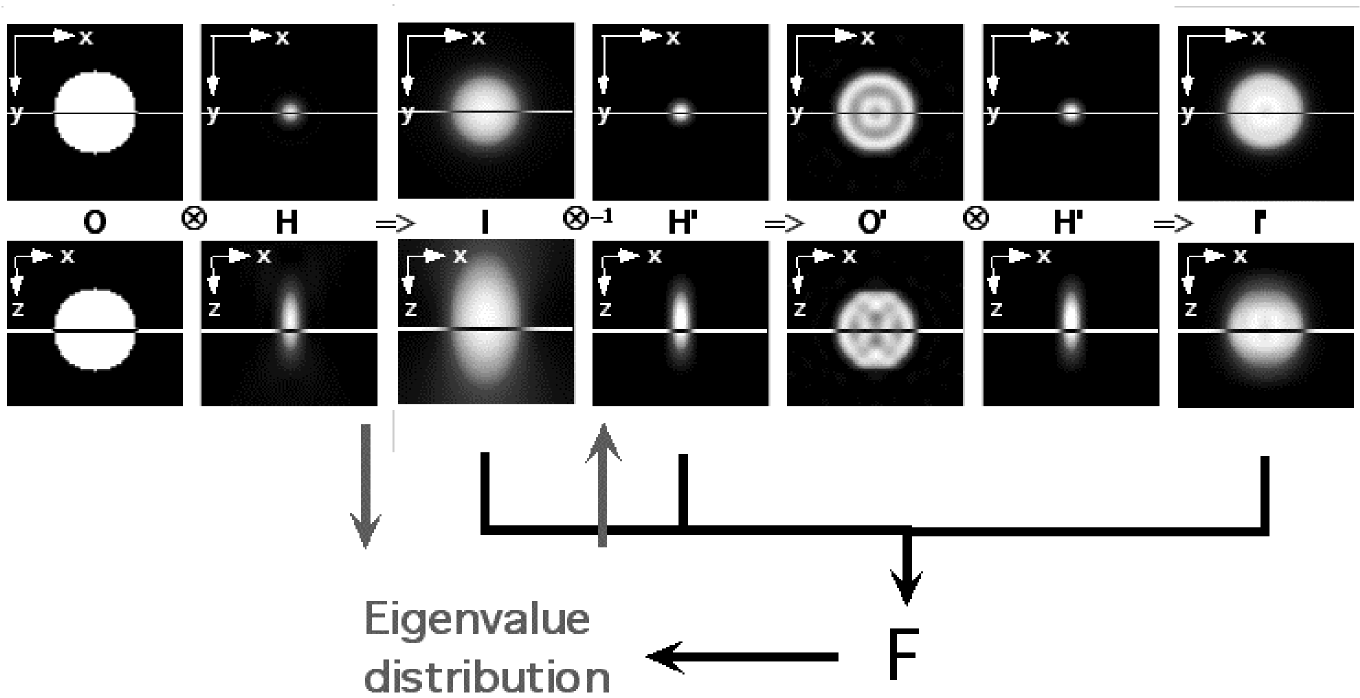

Figure 1

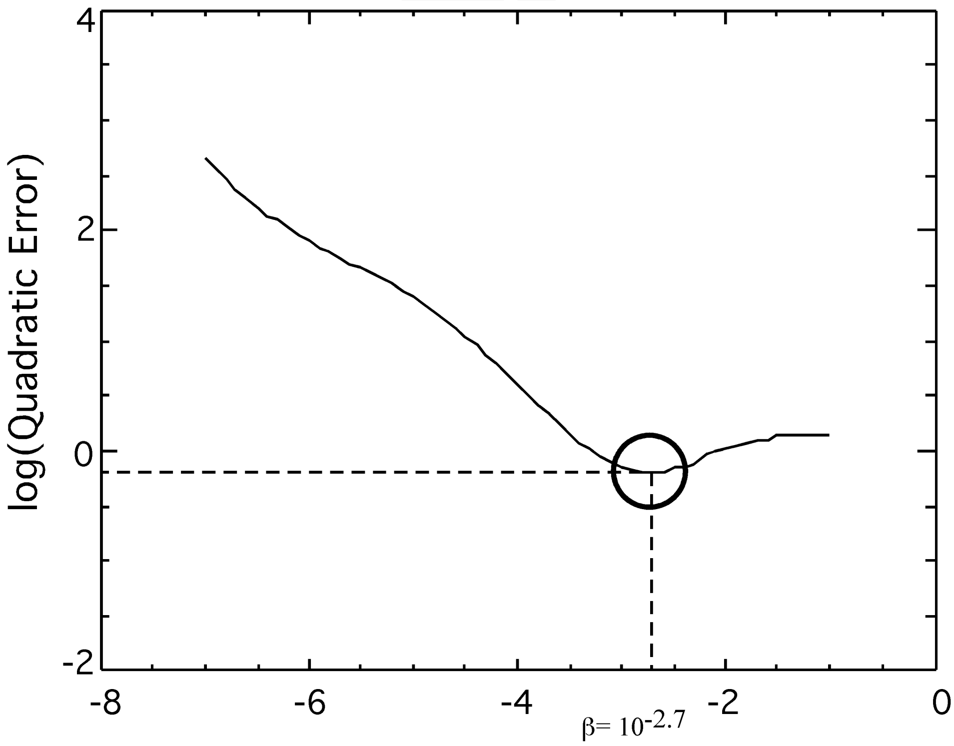

Figure 2

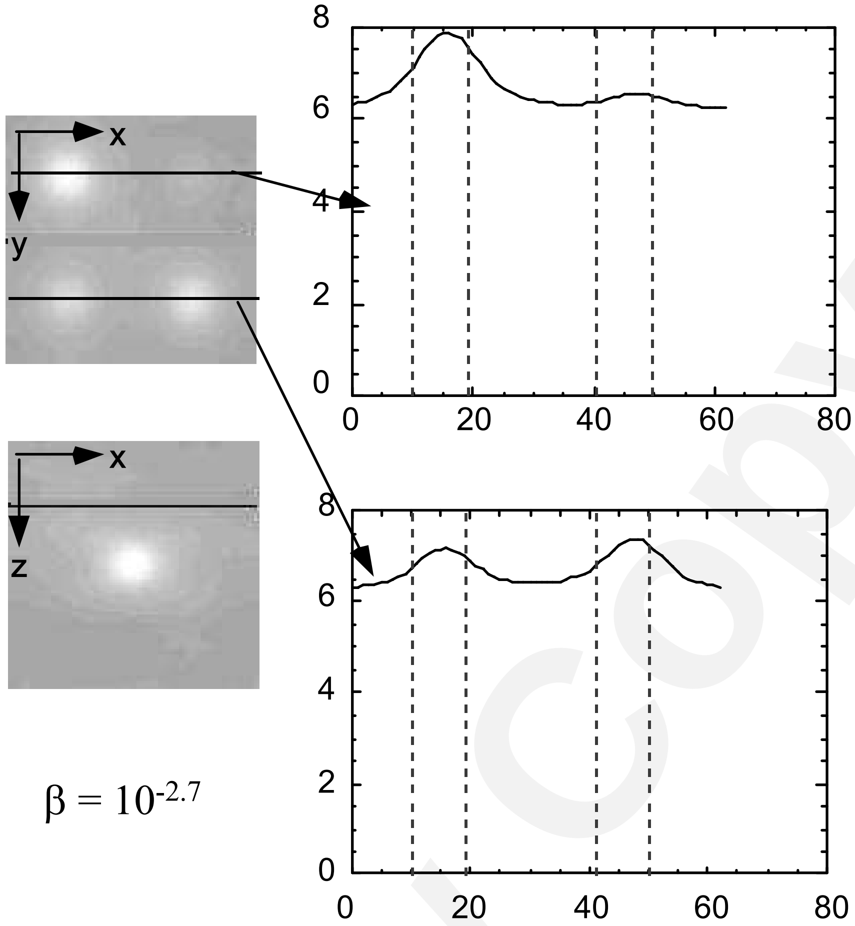
x
y
x
z
β = 10^-2.7
8
6
4
2
0
0
20
40
60
80
8
6
4
2
0
0
20
40
60
80

Figure 3

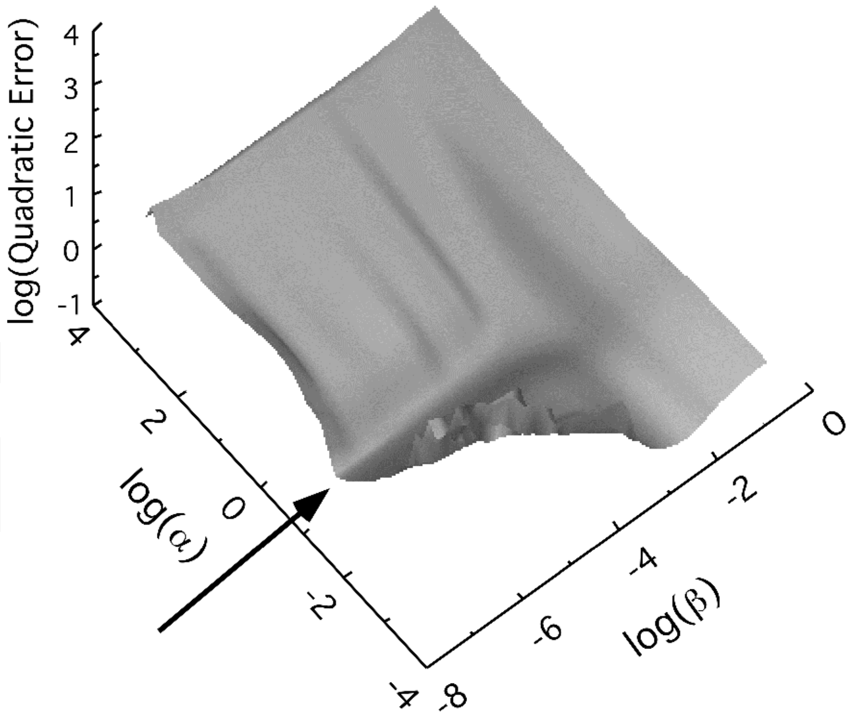
log(Quadratic Error)
4
3
2
1
0
-1
4
2
0
-2
-4
log(α)
-8
-6
-4
-2
0
log(β)

Figure 4

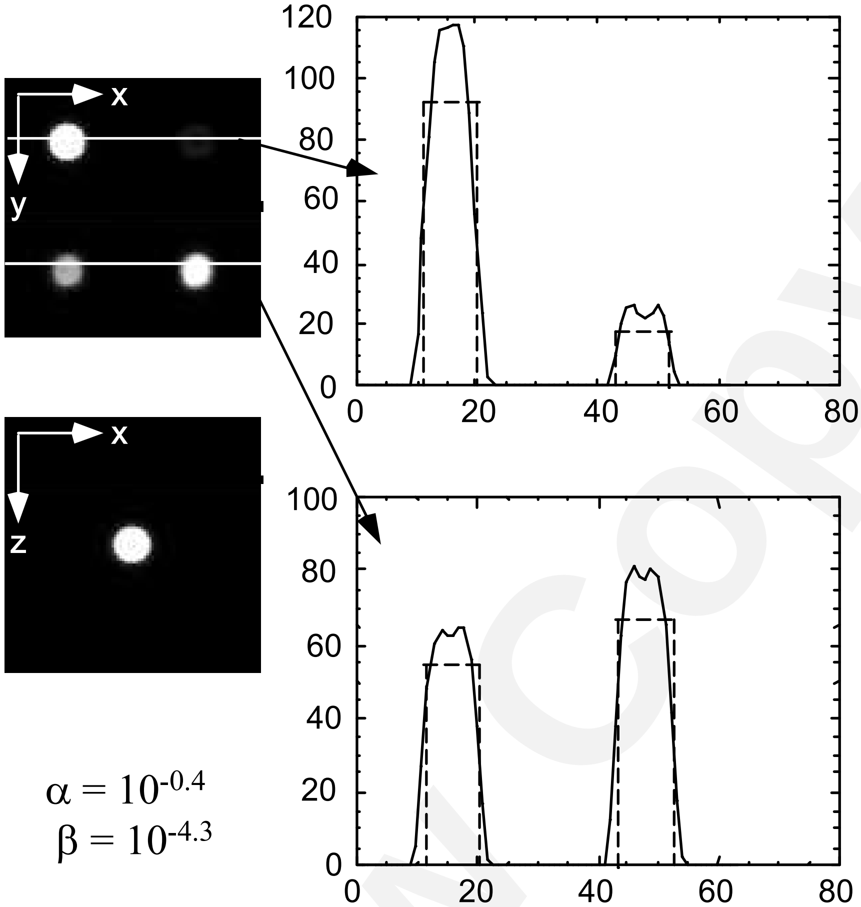

Figure 5

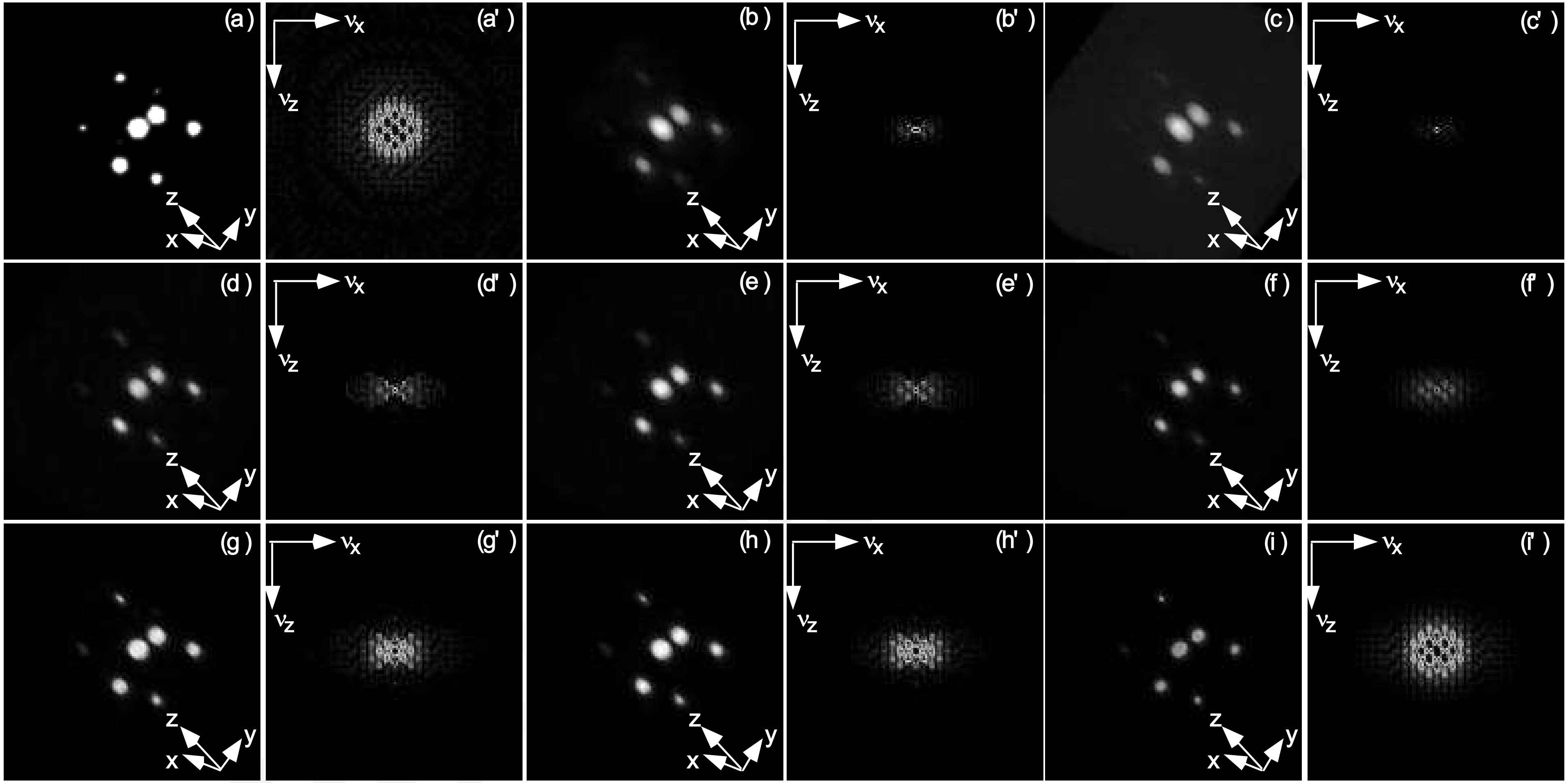

Figure 6

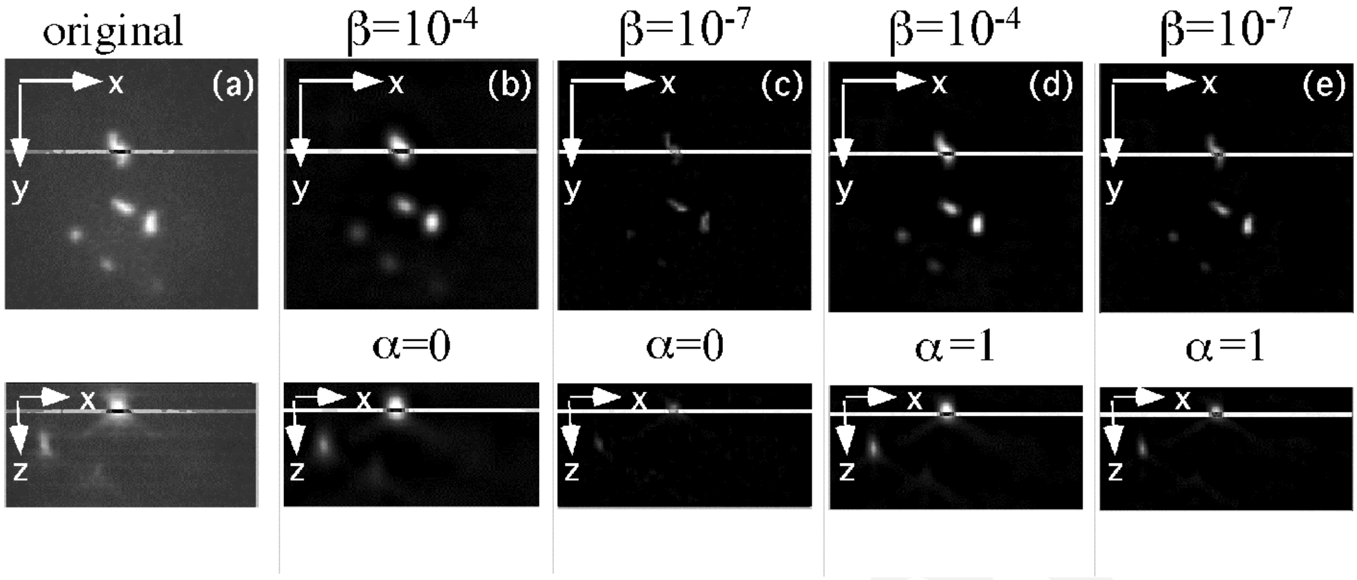

Figure 7